Journal of Applied Fluid Mechanics, Vol. 15, No. 5, pp. 1361-1376, 2022.
Available online at www.jafmonline.net, ISSN 1735-3572, EISSN 1735-3645.
https://doi.org/10.47176/jafm.15.05.1069

Effect of Contact Angle Hysteresis on Evaporation Dynamics of a Sessile Drop on a Heated Surface

X. M. Ye[1], N. K. Zhang[1], R. Cheng[2] and C. X. Li[1†]

[1]*Hebei Key Laboratory of Low Carbon and High Efficiency Power Generation Technology, North China Electric Power University, Baoding 071003, China*
[2]*Patent Examination Cooperation (Tianjin) Center of the Patent Office, CNIPA, Tianjin 300304, China*

†*Corresponding Author Email: lichunxi@ncepu.edu.cn*

(Received January 4, 2022; accepted April 29, 2022)

ABSTRACT

Contact angle hysteresis (CAH) is a significant factor affecting the drop motion on solid substrates. A model of CAH is introduced to explore the influence of CAH on the dynamics of a sessile drop on a uniformly heated surface, and a two-dimensional evolution equation of the drop thickness is established using the lubrication approximation and Navier slip boundary conditions. A numerical simulation is performed to examine the dynamic behaviors of an evaporating drop, and the drop profile, contact angle, contact line, and moving speed are investigated. Simulated results indicate that the drop evolution process involves drop spreading, pinning, and depinning of the contact line. In the drop spreading stage, when the hysteresis angle increases, the spreading period is shortened, and the spreading radius and spreading speed are reduced; in contrast, the pinning period is raised, and the mass of the drop is apparently reduced with increasing hysteresis angle. In the depinning stage, the CAH declines the contact angle, and a flatter pattern is evolved, thereby improving the heat transfer performance, promoting drop evaporation, and shortening the depinning time. The presence of CAH can speed up the drying of the drop, and the large hysteresis angle leads to faster evaporation. Regulating the CAH is an effective way to manipulate the motion of the contact line for an evaporating drop.

Keywords: Drop; Contact angle hysteresis; Evaporation; Contact line pinning; Lubrication theory.

NOMENCLATURE

a	accommodation coefficient	T_i^*	interfacial temperature
Bi	Biot number, $Bi=\frac{H^*h_g^*}{\lambda^*}$	T_s^*	saturation temperature of the liquid
Bo	Bond number	u^*	horizontal velocity
Ca	capillary number	U^*	characteristic velocity, $U^*=\frac{S^*H^*}{\mu^*L^*}$
E	evaporation number	w^*	vertical velocity
H^*	the initial maximum thickness of the drop	β	slip length, $\beta=\frac{\beta^*}{H^*}$
J^*	evaporative mass flux at the interface	β^*	slip length
J_0	$J_0=\frac{\lambda^*(T_m^*-T_s^*)}{H^*L_a^*}$	γ_0	heating parameter, $\gamma_0=\frac{T_w^*-T_s^*}{T_m^*-T_s^*}$
K^*	interface thermal resistance, $K^*=\frac{T_s^{*3/2}}{a\rho_v^*L_a^*}\cdot\left(\frac{2\pi R_g^*}{M_m^*}\right)^{1/2}$	ε	aspect ratio of the drop
L_a^*	latent heat of evaporation.	θ	dynamic contact angle

M_m^*	molecular weight of the vapor	κ^*	mean curvature of the free surface, $\kappa^* = -\nabla^* \cdot \mathbf{n}^*$
$\mathbf{n}^*$	the outward unit normal vector, $\mathbf{n}^* = (-h_{x^*}^*, 1)/\left(1+h_{x^*}^{*2}\right)^{1/2}$	λ^*	the thermal conductivity of liquid at the liquid-gas interface
p^*	pressure	μ^*	dynamic viscosity
R_g^*	universal gas constant	ρ^*	density
S^*	spreading parameter, $S^* = \sigma_{\mathrm{lg},T_s^*}^* - \sigma_{\mathrm{lg},T_m^*}^*$	σ_i^*	surface tension at lg, ls, and sg interface
t^*	time	Ω_i	interfacial tension sensitivity on temperature.
T^*	temperature	$*$	dimensional parameters

1. INTRODUCTION

The evaporation of drops on solid surfaces is ubiquitous in daily life. Proper understanding and manipulation of drop motion on solid substrates are essential for practical applications (Wijshoff 2010; Yin *et al*. 2020; Bonn *et al*. 2009), such as accelerating the cooling rate of microelectronic components, improving the quality of spraying, and improving the accuracy of medical diagnosis. Besides drop evaporation is widely used in industrial and medical fields, e.g., coating process, welding technology, ink printing, and DNA analysis (Lee *et al*. 2008; Matar and Craster 2009; Dugas *et al*. 2005; Kavehpour *et al*. 2002).

Recent studies have shown that the dynamics of drops are strongly dependent on the temperature of solid surfaces (Putnam *et al*. 2012), liquid properties (Ye *et al*. 2018), substrate materials (Lopes and Bonaccurso 2012), and environmental conditions (Kiper *et al*. 2015; Saada *et al*. 2010; Sefiane *et al*. 2009). In addition, the contact angle hysteresis (CAH) (Nagy and Škvarla 2013; Xu and Wang 2020; Eral and Oh 2013) on an actual surface is also a crucial factor affecting the drop movement. Theoretically, the equilibrium contact angle between an ideal surface and a drop attached to it is uniquely determined by Young's equation. It, however, is difficult to measure the exact angle experimentally. The contact angle value is not unique on a solid surface, but changes between two relatively stable angles called the contact angle hysteresis phenomenon. The upper and lower limits are reached at the advancing and receding contact angles (θ_a and θ_r), respectively. The investigation of Neumann and Good (1972) showed that contact angle hysteresis could stem from surface roughness (Johnson and Dettre 1964), chemical heterogeneity (Dettre and Johnson 1965; Johnson and Dettre 1964), and metastable surface energy states. Eral and Oh (2013) found other influential factors, including molecular rearrangement on wetting, interdiffusion, liquid adsorption and retention, and surface deformation.

Many experiments have explored the actual evaporation process of drops. (Yu *et al*. 2004) conducted the evaporation experiment of micro-droplets on the self-assembled molecular layer and found that the evaporation mode switching was attributed to the existence of CAH on an existing surface. Lin *et al*. (2016) experimentally inspected the behaviors of the evaporation of water droplets on polymethyl methacrylate (PMMA) surfaces with six surface roughnesses. They found that the mode transiting from constant contact radius (CCR) to constant contact angle (CCA) was delayed, and the receding contact angle also decreased when increasing the surface roughness. Similar experiments were conducted by Trybala *et al*. (2013) using sessile droplets of the aqueous suspensions containing inorganic nanoparticles on three wetting substrates (PE, PTFE, and silicon wafers). Their results demonstrated that the droplet evaporation exhibited CCR and CCA stages or only CCR when the static contact angle did not reach the receding contact angle. A comparison of the primary behaviors predicted for the pure water evaporation presented a good agreement on all substrates used, with the only difference in the values of static advancing and receding contact angles. Kulinich and Farzaneh (2009) also explored typical evaporation modes on the super-hydrophobic substrates with a similar CA (≥150°) and various CAH. The CCA mode was detected on a low-hysteresis substrate for a high-hysteresis substrate. The evaporation behaviors of a sessile water droplet were not dominated by a high CA but the wetting hysteresis (or receding contact angle). Li *et al*. (2013) found that the contact line pinning was dependent on CAH and was the essential condition for the appearance of a coffee ring stain. Hence, CAH directly influenced the droplet evaporation mode, thereby affecting the deposition mode. It implies that the long-term adhesion of liquid droplets to the solid surface is attributed to CAH. Kuznetsov *et al*. (2016) inspected the evaporation dynamics of a distilled water drop on copper substrates with various roughnesses. They found that the contact radius and duration period of contact line pinning increased with the roughness, and the spreading process can be regulated by changing the substrate roughness. Bormashenko *et al*. (2011) examined the evaporation dynamics of water droplets deposited on a polymer surface and a metal surface. They found that an evaporating droplet exhibited particular behaviors, characterized by stick-slip sliding on weak pinning (polymer) surfaces and a more considerable contact angle hysteresis on strong pinning (metallic) surfaces.

To the best of our knowledge, some theoretical models can predict the entire process of drop

movement on a solid substrate, including spreading, recoiling, pinning, and depinning. However, CAH is seldom considered in these models. Pournaderi and Emdadi (2019) used the sharp method for modeling interface to simulate the impact of droplets on a flat wall. Different contact angle models, proposed by Hoffman (1974) and Jiang *et al.* (1979), separately, without considering CAH, were applied and compared at low and high impact velocities. The results of comparison vary with the impact velocity and surface wettability. Most of the mathematical models in which CAH is considered are employed for describing various stages of contact line motion (Semenov *et al.* 2012; Hu and Wu 2016). These models originated from an equation of the evaporation flux of a sessile droplet, in which a function of the contact angle, $F(\theta)$, has to be determined before solving these models. These models also include two variables, the contact angle, and the contact radius, while results of different stages are obtained by setting either the contact radius or contact angle as constant. Semenov *et al.* (2012) substituted the average surface temperature of droplets instead of the ambient temperature into a formula of total evaporation flux for a water droplet based on their former computer simulations. An equation of contact angle established by Picknett and Bexon (1977) was used in their study. When the radius of the contact line or the contact angle was constant and equal to its initial value, the results obtained for the CCR stage and CCA stage were validated against available experimental results and presented good agreement. Hu and Wu (2016) used a closed-form approximated formulation of the contact angle $F(\theta)$ in the volume evolution model of a tiny sessile evaporating droplet in the stick-slip mode. Two different equations described the contact angle and contact radius evolution behaviors for the CCR and CCA stages. Again good agreement is obtained between the prediction and the experimental data from the literature for droplets evaporating on hydrophilic and hydrophobic surfaces. Although these models can separately bring the dynamics of each stage, the essential dynamic information describing the transition from one stage to the next could be ignored (Pham and Kumar 2019).

The consideration of CAH is reported in investigating a sessile droplet evaporation process by the mesoscopic method, LBM, which has the advantage of automatically tracking interface changes. Ding and Spelt (2007) present a way to regulate the surface wettability in LBM by assuming a CAH window $[\theta_r, \theta_a]$. Based on Ding and Spelt's work, Zhang *et al.* (2021) presented an axisymmetric LBM model to examine the droplet evaporation on a heated surface. They found that the CAH leads to the sequential emergence of the CCA, the CCR, and the mixed modes.

Additionally, many scholars have investigated the dynamics of droplets based on the lubrication approximation. The evolution equation of film thickness, usually one-dimensional, is derived from continuity, momentum, and energy equations. The contact line singularity can be addressed by two methods, the first of which is introducing the microscopic adsorbed film at the contact line, also called the precursor film, and the second of which is using the slip boundary at the liquid-solid interface. The spreading dynamics of the contact angle and the spreading radius are obtained numerically by solving the evolution equation of film thickness. Ajaev (2005) developed a mathematical model using the lubrication theory and the precursor model for the spreading of a thin, volatile droplet on a uniformly heated substrate, suitable for both perfectly wetting and partial wetting liquids. The thickness of the precursor film was determined by the balance of the disjoining pressure and evaporation. The results showed that the contact angle changes slightly over a much larger period and then rapidly decays during a much shorter period, according to the experiment results in the literature. Craster *et al.* (2009) established a continuum model to investigate the dynamics of a slender, evaporating droplet containing nanoparticles and utilized the lubrication approximation to formulate a set of coupled evolution equations of the film thickness and the nanoparticle concentration. Using the precursor film model, they found that a droplet displayed plentiful behaviors involving spreading, evaporation-driven retraction, contact line pinning, and "terrace" formation. Karapetsas *et al.* (2016) also employed the precursor film model to reveal the influence of an insoluble surfactant and non-interacting particles on the dynamic behaviors of evaporating droplets. A relationship of the dynamic viscosity with the local particle concentration was considered. They found that surfactants retarded the evaporation rate of droplets by impeding the motion of the contact line; for droplets containing particles, the droplet lifetime depended weakly on the initial particle concentration and the deposition mode of the particles was affected by the surfactant. The precursor film method and the lubrication approximation (LA) were also employed to investigate the evaporation of multi-component sessile droplets by Diddens *et al.* (2017). Their results showed that compared with the finite element method (FEM), considering the corresponding stokes flow, the LA calculations have a qualitatively similar flow field as the FEM results obtained from the same initial droplet shape when the contact angle is less than 25°. The relative error of the velocity between LA results and FEM results increases with the initial contact angle but is less than 20%.

The method of directly modeling contact line movement, instead of using a precursor model based on the slip boundary condition and lubrication theory, was present by Karapetsas *et al.* (2013) in the study of the dynamics of a droplet on an inclined, non-isothermal solid surface. The moving speed of the contact line is related to the difference between the dynamic and equilibrium contact angles, and the equilibrium contact angle is allowed to change dynamically with the local substrate wettability during the droplet motion. Inspired by the work of Karapetsas *et al.* (2013), Ye *et al.* (2019) numerically examined the dynamics of a sessile evaporating drop on a heated substrate. They discussed the influence of the interfacial tension temperature sensitivity at liquid-gas, solid-gas, and liquid-solid interfaces on substrate wettability and motion behaviors. Their

results documented that variation in sensitivity coefficients is responsible for various evolution features. It effectively manipulates the contact line's motion by altering the temperature sensitivity at the solid-gas interface.

The experiments mentioned above verified that the CAH presents a significant impact on the evaporation dynamics of drops. And some critical dynamic features in the transition stage could be ignored in the way of establishing specific evaporation models, which are empirical at different stages and incomplete. Although the theoretical models based on the lubrication approximation can make up for these drawbacks and describe the entire evaporation process, these models established on ideal surfaces neglect the influence of CAH, leading to the theoretical prediction deviating from the experimental results some extent. To perfect the theoretical model and fully characterize the actual evaporation kinetics of droplets, therefore, in this study, considering the influence of CAH, a two-dimensional drop thickness evolution equation is established using the lubrication approximation and slip boundary conditions. The drop evaporation is numerically simulated to investigate the influence of CAH on the entire drop evaporation process and important parameters, including the contact line, contact angle, moving speed of the contact line, and evaporation time. The physical mechanism of CAH affecting the dynamic evaporation process is discussed.

2. PROBLEM FORMULATION

2.1 Mathematical Model

2.1.1. A quasi-steady evaporation model

We consider the evaporation dynamics of an incompressible drop on an impermeable and horizontal solid surface that is uniformly heated. As shown in Fig. 1, the initial maximum thickness of the drop is H^*, the characteristic length is L^*, and the wall temperature is T_w^* . The magnitude of H^* and L^* in Fig. 1 is only for clarity and does not represent the actual ratio. The superscript "*" indicates dimensional parameters. In this study, we adopt the lubrication theory (Oron *et al*. 1997), which is also employed by Karapetsas *et al*. (2011) and Craster *et al*. (2009) in their modeling to study the drop dynamics.

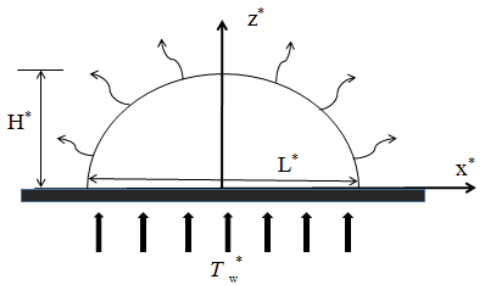

Fig. 1. Diagram of a drop disposited on a horizontal heated substrate.

Referring to Ye *et al*. (2019), by applying the scaling and the lubrication approximation to the continuity, momentum, and energy equations, fluid flow is governed by the following dimensionless equations:

$$\frac{\partial u}{\partial x}+\frac{\partial w}{\partial z}=0 \tag{1}$$

$$\frac{\partial p}{\partial x}=\frac{\partial^2 u}{\partial z^2} \tag{2}$$

$$\frac{\partial p}{\partial z}=-\varepsilon Bo \tag{3}$$

$$\frac{\partial^2 T}{\partial z^2}=0 \tag{4}$$

And the solutions of the above equations are subject to the following boundary conditions. At the liquid-solid interface, we utilize the non-penetration condition, which is as follows,

$$z=0\ ,\ w=0 \tag{5}$$

and the Navier-slip model to address the stress singularity at the contact line,

$$u=\beta\frac{\partial u}{\partial z} \tag{6}$$

where β denotes a slip length, the value is set as 1×10^{-5} referred to in the study of Karapetsas *et al*. (2013)**.** The temperature of the solid surface is assumed to be fixed as

$$T=\gamma_0 \tag{7}$$

Simplified by the tangential and normal stress balance to the liquid-gas interface, we have

$$z=h\ ,\ \frac{\partial u}{\partial z}=\frac{\partial \sigma_{\mathrm{lg}}}{\partial x} \tag{8}$$

$$p=-Ca\frac{\partial^2 h}{\partial x^2} \tag{9}$$

The dimensionless forms of the kinematics and the heat flux at the liquid-gas interface are given as:

$$\frac{\partial h}{\partial t}+u\frac{\partial h}{\partial x}=w-EJ \tag{10}$$

$$\frac{\partial T}{\partial z}=-J \tag{11}$$

The dimensionless evaporation flux at the liquid-gas interface is dependent on the dimensionless temperature here, which is formulated as:

$$KJ=T_i \tag{12}$$

The dimensionless constitutive relation is described as

$$\sigma_i=\sigma_{i,T_s}\left(1-\Omega_i T\right)\ \ (i=\mathrm{lg,\ ls,\ sg}) \tag{13}$$

Integrating Eq. (4) with the temperature boundary conditions of Eq. (7) and Eq. (12) yields the

expression of the surface temperature of the drop and the evaporation flux, expressed as Eq. (14) and Eq. (15), respectively.

$$T_i = -\frac{\gamma_0}{K+h}h + \gamma_0 \tag{14}$$

$$J = \frac{\gamma_0}{K+h} \tag{15}$$

The drop height evolution equation is obtained by the integration method,

$$\frac{\partial h}{\partial t} = \frac{\partial}{\partial x}[-Ca\frac{\partial^3 h}{\partial x^3}\left(\frac{h^3}{3}+\beta h^2\right)+\varepsilon Bo\left(\frac{h^3}{3}+\beta h^2\right)\frac{\partial h}{\partial x}- \frac{\Omega_{lg}K\gamma_0}{(K+h)^2}\frac{\partial h}{\partial x}\left(\frac{h^2}{2}+\beta h\right)]-\frac{E\gamma_0}{K+h} \tag{16}$$

The right side of Eq. (16) represents the impacts of the capillary force, gravity, the thermocapillary force, and the evaporation during the motion of drops, respectively. When $K = E = 0$, Eq. (16) can be simplified into the model without evaporation built by Karapetsas *et al.* (2013).

2.1.2. Contact angle hysteresis model

The advancing contact angle is the critical angle when the three-phase line begins to expand to the unwetted area, reflecting the wetting process of the liquid on solid surfaces. The critical angle when the three-phase line begins to shrink to the wetted area is called the receding contact angle, indicating the dewetting phenomenon of drops on solid surfaces. The difference between the advancing and receding angles is defined as the hysteresis angle of $\Delta\theta$.

For a drop deposited on an ideally smooth substrate, the tangential interfacial forces at the contact point are balanced with Young's equation (Nagy and Škvarla 2013),

$$\sigma_{sg}^*(x_c) = \sigma_{lg}^*(x_c)\cos\theta_e^* + \sigma_{ls}^*(x_c) \tag{17}$$

where θ_e^* denotes the dimensional equilibrium contact angle of the drop on an ideally smooth substrate.

In the frame of the lubrication theory, the aspect ratio ε of the drop is considered very small hence the equilibrium contact angle θ_e^* is small too in reality. So θ_e^* is renormalized by using $\cos\theta_e^* \to \cos(\varepsilon\theta_e)$ (θ_e is a new dimensionless variable of $O(1)$), ensuring all variables with the same order of magnitude. Considering $1-(\varepsilon^2\theta_e^2)/2 \approx \cos(\varepsilon\theta_e)$ and combining the scaled form of Eq. (17) and Eq. (13), we obtain

$$\theta_e^{\,2} = [\frac{(\Omega_{ls}-\Omega_{sg})\sigma_{ls,T_s}\gamma_0+(\Omega_{lg}-\Omega_{sg})\gamma_0}{1-\Omega_{lg}\gamma_0}+ -\frac{2}{\varepsilon^2}\frac{C(1-\Omega_{sg}\gamma_0)}{1-\Omega_{lg}\gamma_0}] \tag{18}$$

where $C=\Omega_{sg,Ts}-\Omega_{ls,Ts}-1$.

For introducing contact angle hysteresis, the following linear empirical expressions are used to describe the relationship between the advancing angles/receding angles and the hysteresis angles (Schulze *et al.* 1989):

$$\theta_a = \theta_e + A\Delta\theta \tag{19}$$

$$\theta_r = \theta_e + (A-1)\Delta\theta \tag{20}$$

where A is a constant related to the liquid properties and not relevant to surface roughness, $A \geqslant 0$. According to the experimental results of water on a stainless-steel surface conducted by Wang *et al.* (2003), the value of A is set to 0.39.

The thickness of the drop at the contact line is zero, that is, h (x=x_{cl}=x_{cr}, t) = 0, where x_{cl} and x_{cr} represent the location of the left and right contact lines, respectively. We use the following empirical expression of a power-law form (Anderson and Davis 1995; Smith 1995), which represents the dependence of the moving speed of the contact line on the local contact angle, to evaluate the contact line speed. (The subscript "c" indicates the contact line.)

$$\upsilon_c = \frac{\mathrm{d}x_c}{\mathrm{d}t} = \begin{cases} B(\theta-\theta_a)^m, \theta > \theta_a \\ -B(\theta_r-\theta)^m, \theta < \theta_r \end{cases} \tag{21}$$

Two constants are noted in Eq. (21): B and mobility exponent of m. We set m = 3 and B = 0.001 in the present calculation referred to the studies of Anderson and Davis (1995) and Karapetsas *et al.* (2013). θ is the dynamic contact angle. $\upsilon_c > 0$ denotes spreading, whereas $\upsilon_c < 0$ denotes receding.

2.1.3. Heat transfer calculation model

The heat flux at a location can be expressed as

$$q^* = -\lambda^*\nabla^* T^* = J^* L_a^* \tag{22}$$

where q* denotes the surface heat flux normalized with the scaling, $q^* = J_0 L_a^* q$, then we obtain

$$q = \frac{\gamma_0}{K+h} \tag{23}$$

2.2 Initial and Boundary Conditions and Meshes

The initial conditions used are formulated as follows:

$$h(x,t=0) = (1-x^2)[\mathrm{H}(1-x)-\mathrm{H}(-1-x)] \tag{24}$$

$$x_{cl}(t=0) = -1,\ x_{cr}(t=0) = 1 \tag{25}$$

where H(x) is the Heaviside function, H(x) = [1+tanh(20x)]/2 (Craster and Matar 2000).

The boundary conditions are

$$h(x=x_{cl},t) = 0,\ h(x=x_{cr},t) = 0 \tag{26}$$

In this study, the coordinate transformation scheme proposed by Karapetsas *et al.* (2013) is employed, then the transient physical domain (x, t) is mapped into a fixed computing domain (x', t').

$$x' = \left(x - x_{\mathrm{cl}}\right)\frac{x_{\mathrm{cr}}\left(t=0\right) - x_{\mathrm{cl}}\left(t=0\right)}{x_{\mathrm{cr}} - x_{\mathrm{cl}}} \tag{27}$$

The drop motion domain of x' is set to [−1, 1], and the time derivative is given by,

$$\frac{\partial}{\partial t} = \frac{\partial}{\partial t'} - \frac{\mathrm{d}x'}{\mathrm{d}t}\frac{\partial}{\partial x'} \tag{28}$$

Eq. (28) is used to replace the corresponding term of Eq. (16). For clarification, the flowchart of the modeling process and numerical method for solving the evolution equation is presented in Fig.2.

A highly efficient solver, Freefem++14.3, is utilized for solving nonlinear partial differential equations based on the finite element method in this simulation. The software provides an advanced automatic mesh generator based on the Delaunay-Voronoi algorithm and a posteriori mesh adaptation. It adopts a general-purpose elliptic solver interfaced with fast algorithms. Hyperbolic and parabolic problems are addressed by iterative algorithms stipulated by users. The sparse matrix storage format is employed to achieve the requirements of low memory and fast calculation speed.

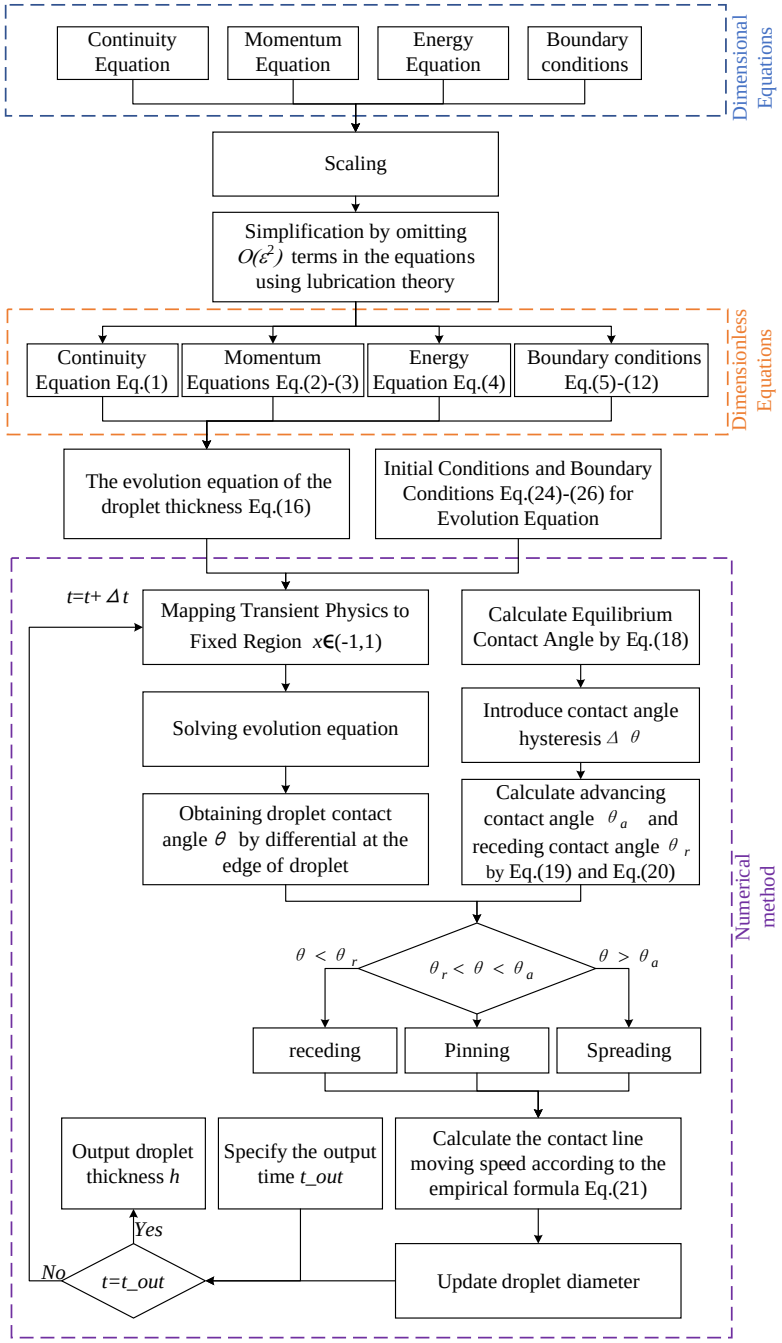

Fig. 2. Flowchart of the modeling process.

In the present calculation, because the Freefem++ is suitable for two- and three-dimensional computational domain exclusive one-dimensional domain, Eq. (16) is solved in the rectangular area of [0, 2] × [0, 1] in this study. To verify the grid independence, we divide the range of [−1, 1] in the *x*-direction into 300, 500, and 800 grids, respectively, and the range of [0, 1] in the *y*-direction, which has no relation to the evolution equation, is divided into only two grids to save computation time. The residual mass of the drop (m_j) and the dynamic contact angle of the drop (θ_r) at t=70 000 are used as the criteria for justifying the grid independence. The results are presented in Table. 1. With careful consideration, the grid of 500 is selected, ensuring computation efficiency and accuracy.

Table. 1. Grid independence validation

Grid number	m_j	θ_r	Computation time
300	0.04742	0.3508	3.01 hours
500	0.04710	0.3500	4.89 hours
800	0.04690	0.3502	7.98 hours

3. RESULTS AND DISCUSSION

In Eq. (18), Ω_{lg}, Ω_{sg}, and Ω_{ls} represent the sensitivity of liquid-gas, solid-gas, and liquid-solid interfacial tensions to the local temperature. Assume that all sensitivity coefficients are the same, namely, Ω_{lg} = Ω_{sg} = Ω_{ls} =1. Under this condition, the equilibrium contact angle is constant, as described by

$$\theta_e^{\,2} = -\frac{2}{\varepsilon^2}C\,. \tag{29}$$

Karapetsas *et al.* (2013) adopted the same assumption to simulate the thermocapillary motion of a droplet on an inclined substrate and presented the value of C as −0.004. To reveal the influence of CAH on the drop evaporation dynamics and physical mechanism, cases without and with CAH (indicating with $\Delta\theta$ =0 and≠0) will be discussed below. Referring to the experiments conducted by Gatapova *et al.* (2014), the main parameters of the drop are presented in Table. 2, and the range of the dimensionless parameters can be computed, as shown in Table. 3. We choose some values of the parameters from the range in Table 3, which are: ε = 0.1, Bo =0.5, γ_0 = 0.1, Ca = 0.1, K = 10, and E = 1× 10^{-3}. As we mentioned above, some values of constants are set as: A = 0.39, B = 0.001, m = 3, $\sigma_{ls,0}$ = 1, C = −0.004, β = 1×10^{-5}. Then we can know θ_e is 0.894 in radian (all angles calculated are in radian in this study). According to the initial condition, the initial contact angle θ_0 is calculated as 1.1. To ensure the complete presentation of the entire evaporation process, including spreading, pinning, and shrinking, we set the advancing contact angle θ_a to be smaller than the initial contact angle θ_0. Substituting the value of θ_0, θ_e, and A into Eq. (19), we obtain the varying range of CAH as $0 < \Delta\theta < 0.53$. Gatapova *et al.* (2014) and Chu *et al.* (2017) measured the CAH characteristics of various liquid drops on different surfaces and found that the hysteresis angle ranged from 0 to 90°, i.e., 0 to 1.57 in radian. Considering that the angle in the present study is scaled, which means the actual angle in the experiments is enlarged, any value is selected from the range of $0 < \Delta\theta < 0.53$ is reasonable compared to the experiments.

Table. 2. Typical range of dimensional parameters

Parameters	Symbol (unit)	Range
Drop thickness	H^*(m)	(1~5)×10^{-3}
Width	L^*(m)	10^{-2}
Liquid viscosity	μ^*(Pa·s)	2.9×10^{-4}~10^{-3}
Liquid density	ρ^*(kg·m^{-3})	10^3
Vapor density	ρ_v^* (kg·m^{-3})	1
Surface tension	σ_{lg}^*(N·m^{-1})	10^{-2}~10^{-1}
Latent heat	L_a(KJ·kg^{-1})	10^3
Thermal conductivity	λ^*(KW·$m^{-1}K^{-1}$)	10^{-4}

Table. 3. Definition and range of nondimensional parameters.

Parameters	Definition	Range
Aspect ratio	$\varepsilon = H^*/L^*$	0.01~0.1
Bond number	$Bo = \dfrac{\rho^* g^* H^{*2}}{\mu^* U^*}$	10^{-1}~10^3
Heating number	$\gamma_0 = \dfrac{T_w^* - T_s^*}{T_m^* - T_s^*}$	0~1
Evaporation number	$E = \dfrac{\lambda^{*2}\left(T_m^* - T_s^*\right)}{\varepsilon H^* U^* \rho^* L_a^*}$	10^{-5}~10^{-1}
Capillary number	$Ca = \dfrac{\varepsilon^2 \sigma^*_{\mathrm{lg},T_m^*}}{S^*}$	10^{-2}~10^{-1}
Temperature sensitivity coefficients	$\Omega_i = \dfrac{\xi^*_{1T_i^*}\left(T_m^* - T_s^*\right)}{\sigma^*_{i,T_s^*} - \sigma^*_{\mathrm{lg},T_m^*}}$	0~10
Interfacial thermal resistance	$K = \dfrac{\lambda^* K^*}{\varepsilon L_a^* L^*}$	0.1~10

3.1 Effect of CAH on Drop Evaporation

Firstly, the effect of CAH on drop evaporation is evaluated in this section. A moderate value of $\Delta\theta$, 0.27, from the range mentioned above, is chosen for the case with CAH, then θ_a=0.999, θ_r=0.730 according to Eq. (19) and Eq. (20). As the case ignoring the effect of CAH, $\Delta\theta$ =0, we have θ_a = θ_r = θ_e = 0.894. For a drop spreading on a solid surface with uniform temperature, the symmetrical behaviors are illustrated around the drop center of x = 0. Therefore, the contact angle and line on the right side are selected to display the detailed dynamic features. The evolution characteristics of the drop are illustrated in Figs. 3~5. Fig. 3 illustrates the drop profiles without and with CAH, respectively. It is found that the spreading range of the drop is very limited; compared to the case without CAH, the

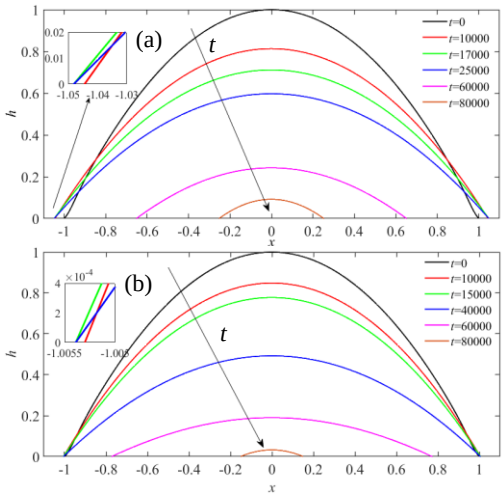

Fig. 3. Profile of the drop evolution: (a) without CAH (Δθ=0); (b) with CAH (Δθ=0.27).

spreading radius of the drop with CAH is reduced slightly, the overall shape of the drop is seen to be thicker during spreading, while the retraction starts later and the drop profile is thinner and flatter in the contact line depinning stage, e.g., t = 80 000. To further examine the impact of CAH, Fig. 4 depicts the variations in typical parameters of the drop evaporation process with and without CAH. The drop evolution process in both cases can be classified into three stages: drop spreading, contact line pinning, and depinning (Fig. 4b and Fig. 4c), but the parameter variation and duration of each stage are significantly different (Fig. 4c). Table. 4 summarizes the vital moment and the period of drop evaporation in two cases.

In the spreading stage, the contact angle reduces slightly (Fig. 4a), the contact line spreads outward (Fig. 4b), and the spreading velocity gradually slows down (Fig. 4c). When considering the CAH, the spreading time is shortened from t = 0~17 000 to 0~15 000. The growth rate of the drop spreading diameter at this stage can be expressed as the power-law relation between (x_{cr}–x_{cl}) and t, namely, the drop with Δθ=0 and Δθ=0.27 satisfy (x_{cr}–x_{cl}) ~ $t^{0.02}$ and ~ $t^{0.002}$, respectively, that is, CAH significantly reduces the spreading velocity and inhibits the spreading process. The maximum spreading radius of the drop can reach 1.05 when Δθ=0, while the spreading velocity is slow and the spreading time is shortened when Δθ=0.27, resulting in a smaller spreading radius of about 1.0053 (Fig. 4b). The contact angle for Δθ=0.27 is always greater than that for Δθ=0, and the overall spreading of the drop is suppressed significantly.

Table. 4. Evolution moment and stage duration of drops without CAH (Δθ=0) and with CAH (Δθ=0.27).

Δθ	Moment			Stage		
	Pinning	Depinning	Drop vanishing	Spreading	Pinning	Depinning
0	17 000	25 000	93 000	0~17 000	17 000~25 000	25 000~93 000
0.27	15 000	40 000	84 500	0~15 000	15 000~40 000	40 000~84 500

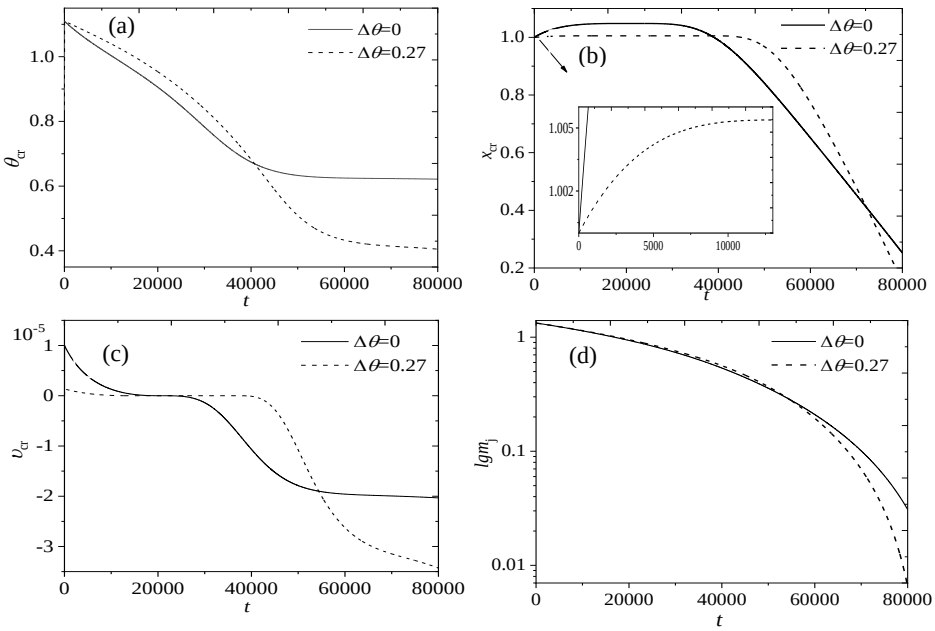

Fig. 4. Variation in the characteristic parameters: (a) dynamic contact angle; (b) contact line position; (c) contact line speed; (d) remained mass.

In the pinning stage, the contact line is fixed, and the contact angle declines continuously. For $\Delta\theta$=0.27, the contact angle decreases from θ_a=0.999 to θ_r=0.730, which is always higher than the dynamic contact angle for $\Delta\theta$=0. For $\Delta\theta$=0, the moving speed of the drop is close to zero, and the contact line can be regarded as pinning, whereas, for $\Delta\theta$=0.27, the contact line is pinned completely, characterized by v_{cr}= 0. Influenced by the CAH, the drop pinning duration increases considerably (Fig. 4b), rising from t = 17 000~25 000 to 1 000~40 000(Table. 4). Bormashenko *et al.* (2011) performed an evaporation experiment of water droplets on the aluminum surface with a hysteresis angle of about 50° and found that the evaporation process is mainly governed by pinning. In this study, a rapid reduction of the drop mass is found in the pinning stage (Fig. 4d), and the drop mass is reduced by 0.49 for $\Delta\theta$=0.27, accounting for 36.83% of the total mass of the initial drop, which is higher than 12.13% for $\Delta\theta$=0. Hence, when considering the CAH, the pinning stage presents a significant impact on the entire drop evolution, which is qualitatively in accord with the experimental data reported by Bormashenko *et al.* (2011).

In the depinning stage, the contact angle reduces rapidly and then slowly. At this moment, the drop continues to retract, and the retracting velocity of the contact line increases quickly and then gradually. The CAH not only accelerates the retracting speed of the drop from $t^{-2.48}$ to $t^{-3.44}$, but significantly shortens the duration of this stage. Namely, the drop retracts from t = 25 000 to t = 93 000 for the case of $\Delta\theta$=0, while the drop for $\Delta\theta$=0.27 begins to retract at t = 40 000, and ends at t = 84 500. Besides, the drop mass decreases quickly from t = 60 000, and the contact radius retracts rapidly. The retracting velocity, v_{cr}=2.62×10^{-5} for $\Delta\theta$=0.27, is higher than v_{cr}=1.96×10^{-5} for $\Delta\theta$=0. It can be inferred from Fig. 4d that CAH can accelerate the evaporation process of drops. For $\Delta\theta$=0.27, the drop is close to being dried at t = 80 000, and the drop mass is 0.00654 at this time; while for $\Delta\theta$=0, the drop mass is 0.0309, which is almost five times as much as that for $\Delta\theta$=0.27. Brutin and Sobac (2015) argued that the drop evaporation rate is closely dependent on the wetting radius and contact angle, that is, a large wetting radius and small contact angle lead to an increase in the evaporation rate. Compared with the case of $\Delta\theta$=0, the evaporation rate is slowed down due to the small spreading radius and the large contact angle for $\Delta\theta$=0.27 in the spreading stage. In the depinning stage, the drop for $\Delta\theta$=0 presents a larger contact angle for a longer time (Fig. 4a), while the retracting radius for $\Delta\theta$=0.27 is more prominent and the contact angle is more small, thereby the drop behaving as a flat shape, and then accelerating the evaporation process. Consequently, it is in the depinning stage that the dynamic characteristics of the contact line have a more noticeable effect on the evaporation process of drops.

The moving speed of the contact line is greater than zero, along with the advancement of the drop. When the moving speed is zero, there are two critical contact angles: the advancing and receding angles. The difference between the two angles is the hysteresis angle (Orlova *et al.* 2018). Figure 5 illustrates the relation of the dynamic contact angle with the moving speed, where the timeline direction represents the direction of the drop movement. It is found from Fig. 5 that similar features are observed for two cases, e.g., the moving speed gradually decreases from a positive value to 0 and then turns to a negative value, and the dynamic contact angle always keeps a decreasing trend as time proceeds. But differences are: for $\Delta\theta$=0.27 when the moving speed is equal to 0, there are two critical angles of 0.999 and 0.73, namely, the advancing angle of θ_a=0.999 and the receding angle of θ_r=0.73, which correspond to the starting moments of contact line pinning and depinning. The trend of the dynamic contact angle considering CAH in this study is in accordance with the experimental study of Orlova *et al.* (2018). For $\Delta\theta$=0, there is only a critical angle of 0.894, that is, θ_a= θ_r= θ_e= 0.894. It indicates that the CAH has a crucial impact on the moving speed during the movement of the drop. Hence, the drop movement and the evaporation process could be regulated by changing the CAH.

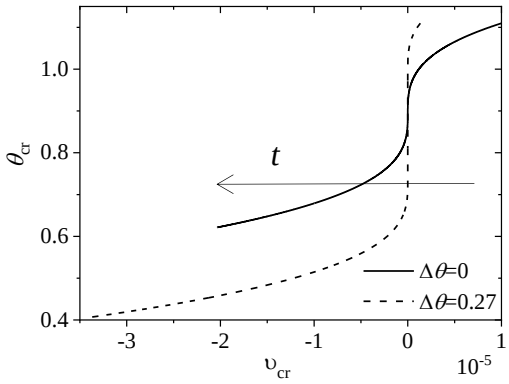

Fig. 5. Relation between the dynamic contact angle and moving speed of the contact line.

Gatapova *et al.* (2014) carried out drop evaporation experiments on the surface coated with hexamethyldisilazane (HMDS) using water drops with the initial volume of 92.6μL under the condition of a temperature difference of 40°C between a substrate and environment. They measured the temporal evolution of the dynamic contact angle and contact line position. Their experimental results are normalized with the substitution of $\theta_e^* \rightarrow \varepsilon\theta$ and then compared with the present simulation, as shown in Fig. 6. A comparison indicates that the present simulated results with CAH coincide with the experiment conducted by Gatapova *et al.* (2014), that is, the theoretical model with CAH could accurately reflect the typical characteristics of the drop movement. It is worth noting that the experiment Gatapova *et al.* (2014) does not show the drop spreading stage, which may be due to the rapid change in this stage and the difficulty of observation and recording.

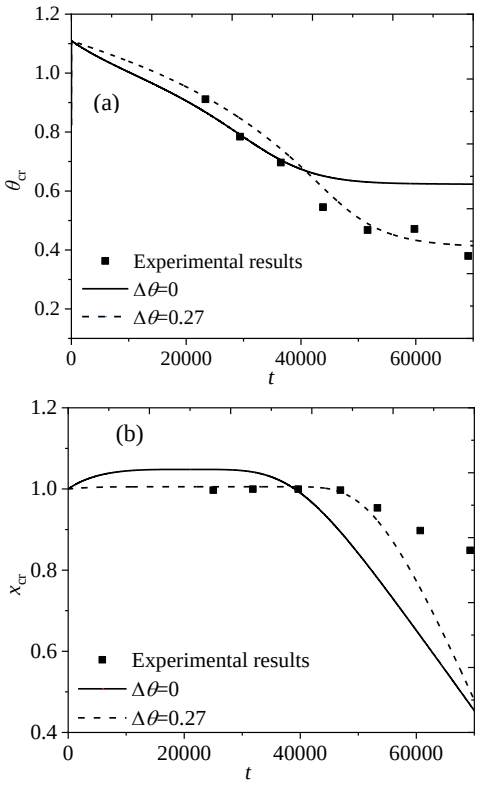

Fig. 6. Comparison of present simulated and experimental results: (a) contact angle; (b) contact line

Eq. (14) shows that the drop surface temperature T is negatively correlated with the local liquid film thickness h, so the surface temperature at the center is the lowest, while the two sides are higher, forming the Marangoni effect from both sides to the center. During evaporation, the primary way of heat transfer is the release of latent heat. It can be seen from Eq. (23) that the distribution of surface heat flux q along the wall direction is similar to the surface temperature T, that is, it shows a variation of a gradually decreasing trend from both sides to the center, as shown in Fig. 7. The experiment of Pasandideh-Fard *et al*. (2001) measured the heat flux distribution of water droplets spreading on a smooth stainless steel surface, and found that the heat flux q gradually increased along the center of the droplet toward the contact line. Pan *et al*. (2020) numerically examined the evaporation of water droplets and found an increase in the local evaporation flux along with the interface toward the contact lines. Hence, the trends of the present results are consistent with the above results, thus verifying the reliability of the two-dimensional surface heat flux model proposed in Section 2.1.3.

Using Eq. (23), setting K to 0.3 and keeping other parameters unchanged, the evolution equation of the film thickness is solved, and the heat flux distribution at the liquid-gas interface is obtained in Fig.7. It illustrates that the drop surface heat flux gradually increases with time for both cases of $\Delta\theta$=0 and $\Delta\theta$=0.27, which can be explained by the gradual decrease in the drop thickness with the drop evaporation. It, however, apparently presents different heat transfer characteristics at various stages for the case of $\Delta\theta$=0 and $\Delta\theta$=0.27. Compared with $\Delta\theta$=0, in the spreading stage, the surface heat flux for $\Delta\theta$=0.27 is smaller, and the heat transfer capacity of the drop is weak, which can be explained by the thick film is not conducive to heat transfer. Taking t = 10 000 as an example, the surface heat flux at x = 0 is reduced by 2.6% compared with the case of $\Delta\theta$=0. In the depinning stage, the surface heat flux for $\Delta\theta$=0.27 is large, and the heat transfer capacity is enhanced, which results from the flat shape that can facilitate heat transfer and promote the evaporation of the drop.At t=80 000, the surface heat flux at x = 0 is increased by 11.1% compared with the case of $\Delta\theta$=0. Kandlikar (2012) concluded that increasing the surface roughness can enhance the heat transfer of a single-phase liquid flow in microchannels, thus confirming that the CAH improves the heat transfer.

From Eq. (15) and Eq. (23), it can be seen that the dimensionless heat flux based on so called one-sided evaporation model equals the dimensionless evaporation flux. Ajaev (2005) presented a typical dimensionless evaporation flux profile for a droplet evaporationg in CCA stage, with the Marangoni

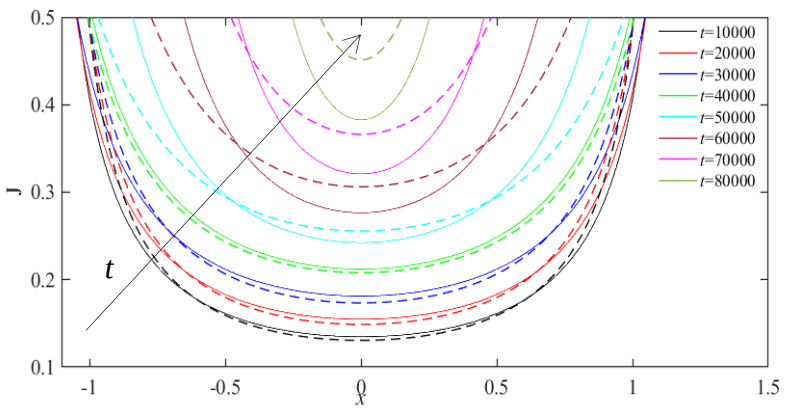

Fig. 7. Distribution of heat flux along with the liquid-gas interface. The solid and dashed lines denote $\Delta\theta$ = 0 and $\Delta\theta$ = 0.27, respectively.

effect, gravity and CAH neglected. So we set Bo=0, Ω_{lg}=0, $\Delta\theta$=0, θ_e=1.2, B=0.04, Ca=10^{-3}, K=0.05 to initiate a droplet evaporation also in CCA stage for comparison calculation. The results of evaporation flux and drop shape at normalized time t/t_e=0.4 are shown in Fig. 8, where t_e is the dimensionless total evaporation time. It can be seen that the drop shape is approximately the same as that of Ajaev (2005) and the present evaporation process is a little faster. The evaporation flux of present result increases sharply when droplet radius exceeds 0.6 and approaches its maximum value near the contact line. Compared with the evaporation flux of Ajaev (2005), present curve is lower due to the different value of parameters used.

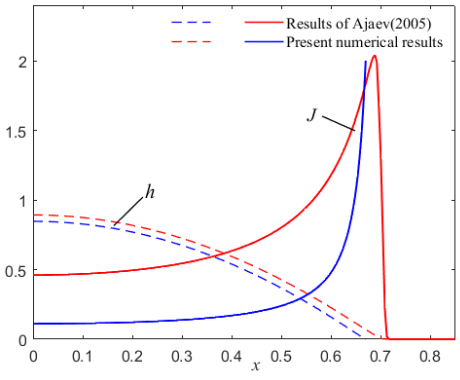

Fig. 8. Comparison of droplet shape and evaporation flux without considering CAH at normalized dimensionless time t/t_e=0.4. Red solid and dashed curves are the results of Ajaev (2005), blue solid and dashed curves are present numerical results.

Eq. (16) displays that drop evaporation is dominated by the capillary effect, gravity effect, the thermocapillary effect, and the evaporation effect. Fig. 9 depicts the variations in four elements at the center and edge of the drop when the CAH is considered to examine the impact of the above factors further. As time continues, the effects of capillary force, gravity, and thermocapillary force gradually weaken (Fig. 9a and Fig. 9c), while the impact of evaporation continues to increase (Fig. 9b and Fig. 9d). At the center of the drop, Fig. 9a and Fig. 9b illustrate that the reduction of drop thickness is strengthened by gravity and evaporation effects; it, however, is impeded by the capillary and thermocapillary effects. At the edge of the drop, Fig. 9c and Fig. 9d show that the capillary, gravity, and evaporation effects promote the reduction of the drop thickness, whereas the thermocapillary force acts as inhibition, and evaporation always plays a significant role. From t = 0 to 15 000, gravity dominates the drop evolution and prompts the drop to spread outward, but the spreading radius is small due to the inhibition of other factors. When t = 15 000~40 000, the drop surface temperature presents an inverse relationship with the drop thickness, thus the evaporation, which is positively correlated with the temperature, gradually increases from the center to the edge, that is, the effect of evaporation at the edge is significantly higher than that at the center (Fig. 9b and Fig. 9d); in addition, temperature increases with the drop thickness at the contact line decreases, thus increasing the local evaporation mass. The supplemented mass toward the contact line induced by the combined contribution of gravity, the capillary and the thermocapillary forces is balanced with the evaporated mass, thereby realizing the dynamic balance manifested as the pinning of the contact line.

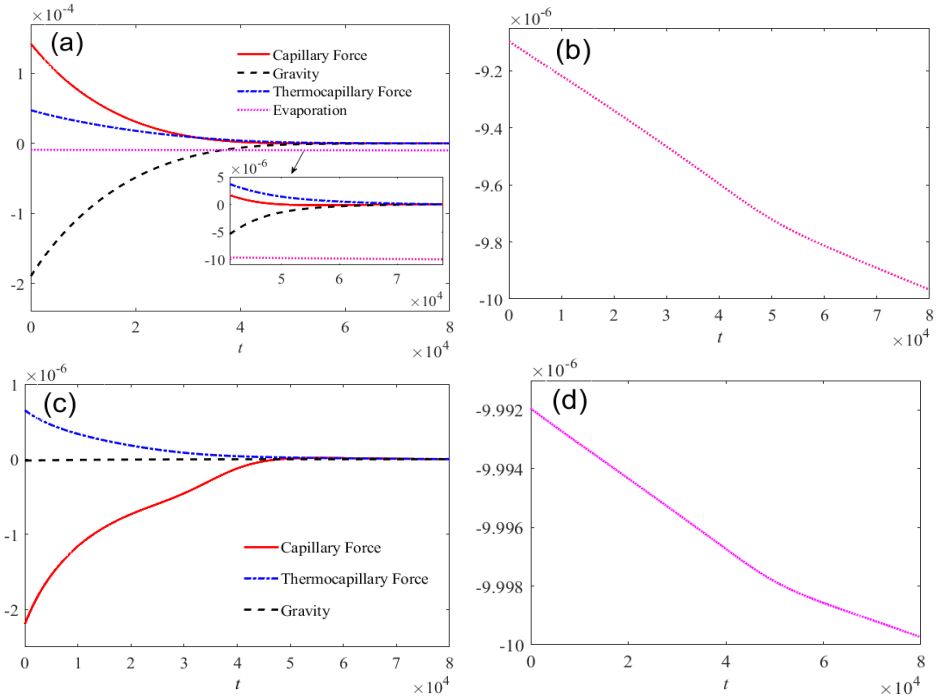

Fig. 9. Variations in different factors during the drop evolution with CAH: (a) variations in four factors with time at the center of drop; (b) magnification of evaporation in (a); (c) variations in three factors with time at the edge of drop; (d) variation in evaporation at the edge of the drop.

In the depinning stage (t = 40 000~80 000), the contribution of the other three factors to the decrease of drop thickness is close to 0, while evaporation plays a leading role. Under this condition, the total mass loss caused by evaporation at the edge is significantly higher than the mass supplement brought by the contribution of the above three forces. The dynamic balance is destroyed, showing a retraction state where the contact line and contact angle are continuously reduced.

3.2 Effect of Different CAHs

To explore the influence of different hysteresis angles on the drop motion, three values of $\Delta\theta$=0.27, 0.39, and 0.48 are used in the following calculation, and other parameters remain unchanged. Fig. 10 illustrates the drop evolution process. In the spreading stage, as the hysteresis angle increases, the spreading radius decreases while the thickness of the drop increases, as shown in Figs. 10a and 10b. However, the drop profile difference is not significant because the surface temperature is low in this stage, and the evaporation rate is slow. Figs. 10c~10e shows that the increase of the hysteresis angle makes the drop retract faster, and the drop thickness decrease in the depinning stage. The surface temperature increases with the time, then the evaporation rate is also raised to some extent, and the drop profile difference gradually emerges; e.g., at t=75 000 (Fig. 10e), the retracting radius is 0.318, 0.278, and 0.217 for $\Delta\theta$=0.27, 0.39 and 0.48, respectively, the drop height is 0.071, 0.044 and 0.017. It can be concluded that as the hysteresis angle increases, the drop retracting radius and height decrease.

Fig. 11 compares the varieties of the main parameters under the three hysteresis angles. It can be noted that the trends of the contact angle, contact line, and moving speed for the three cases are roughly the same. The drop evolution includes spreading, pinning, and depinning, but the starting time and duration of each stage are obviously different, as shown in Table. 5. For $\Delta\theta$=0.39, the moments that the drop starts pinning and depinning are t = 8 000 and t = 44 000, respectively, while for $\Delta\theta$=0.48, are at t = 3 000 and t = 47 000, respectively, namely, the start moment of pinning is advanced, and the depinning is delayed. It reveals that increasing the hysteresis angle prolongs the pinning time of the contact line and shortens the duration of the spreading stage and the depinning stage, thereby speeding up the evaporation process of the drop. As shown in Figs. 11a ~ 11c, as the hysteresis angle increases, the drop spreading radius and velocity decrease during the spreading stage. The maximum drop spreading radius for $\Delta\theta$=0.48 is only 1.00072, which is much smaller than that for $\Delta\theta$=0.27 and $\Delta\theta$=0.39. In the depinning stage, the power-law relationship between the drop retracting diameter (x_{cr}–x_{cl}) and time t is ~ $t^{-3.44}$, $t^{-3.89}$, and $t^{-4.20}$ for $\Delta\theta$=0.27, 0.39, and 0.48, which can be inferred that the increasing hysteresis angle speeds up the drop retracting velocity and then shortens the duration of this stage, as shown in Table. 5.

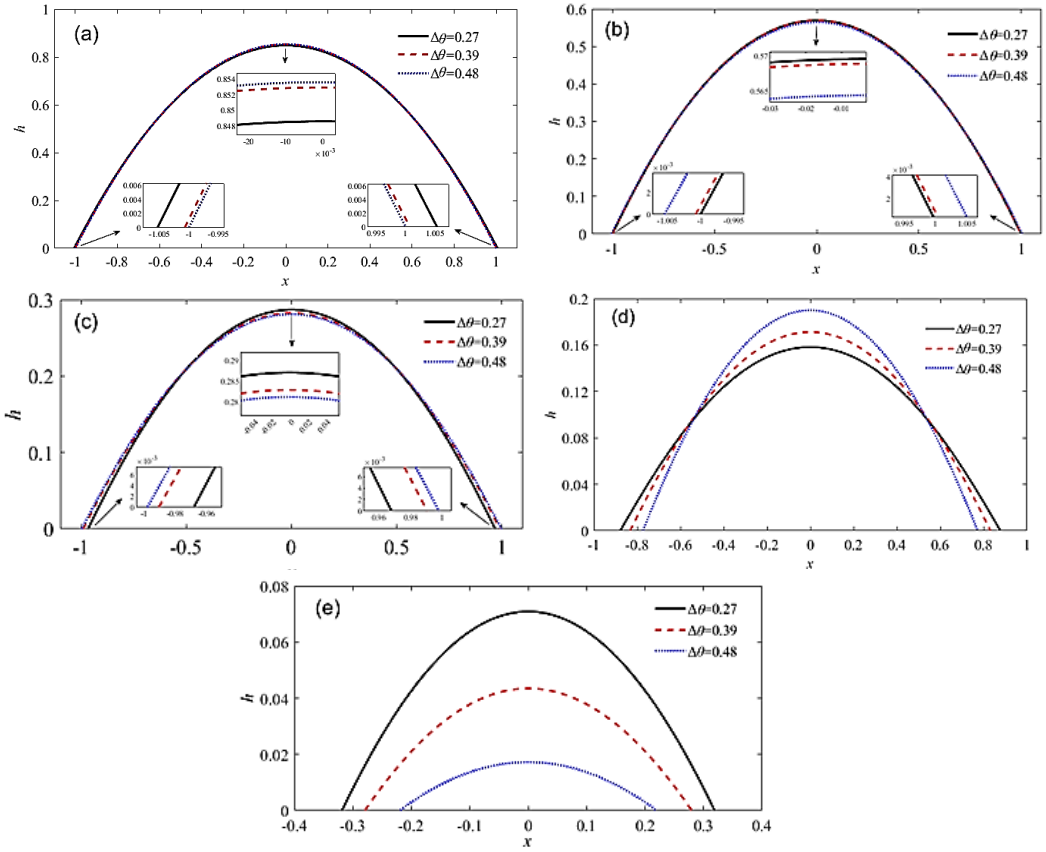

Fig. 10. Drop profile during the drop evolution process: (a)*t* = 10 000; (b) *t* = 30 000; (c) *t* = 50 000; (d) *t* = 70 000; (e) *t* = 75 000.

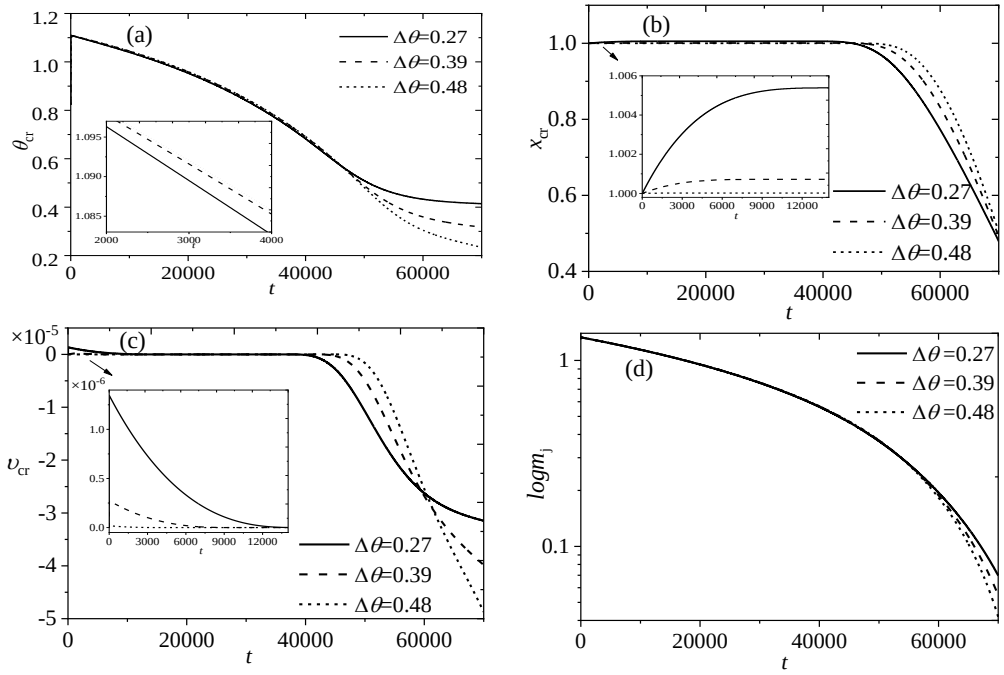

Fig. 11. Variation in the characteristic parameters: (a) dynamic contact angle; (b) contact line position; (c) contact line velocity; (d) remained mass.

Table. 5. Effect of varied Δθ on the drop evolution time.

Δθ	Moment			Stage		
	Pinning	Depinning	Drop vanishing	Spreading	Pinning	Depinning
0.27	15 000	40 000	84 500	0~15 000	15 000~40000	40 000~84 500
0.39	8 000	44 000	81 500	0~8 000	8 000~44000	44 000~81 500
0.48	3000	47 000	78 000	0~3 000	3 000~47000	47 000~78 000

At t = 70 000, the drop mass for Δθ=0.27, Δθ=0.39, and Δθ=0.48 is 0.0697, 0.0535, and 0.0418, respectively, that is, the increase of the hysteresis angle reduces the remained mass of the drop (Fig. 11d), which speeds up the drying process. The reason is possibly attributed to lowering the contact angle owning to the increasing contact angle hysteresis in the depinning stage, and the air circulation near the contact line is weakened (Kulinich and Farzaneh 2009), which makes the drops evaporate faster. On the other hand, the pinning time is prolonged, and the solid-liquid contact diameter increases, accelerating the evaporation process at the drop edge.

Fig. 12 illustrates the relationship between the dynamic contact angle and the moving speed of the contact line under the three hysteresis angles. It can be found that the hysteresis angle has different effects on the entire process, including spreading, pinning, and depinning stages. In the pinning stage, the advancing and receding contact angles of the drop with Δθ=0.27 are θ_a=0.999 and θ_r=0.73, respectively. The drop with Δθ=0.39 and Δθ=0.48 corresponds to θ_a =1.045, θ_r=0.658 and θ_a=1.083, θ_r=0.598, respectively. As shown in Table. 6, as the hysteresis angle increases, the advancing contact angle increases, and the receding contact angle decreases. The reduction in the receding contact angle is greater than an increase in the advancing contact angle, which is consistent with the investigation of Schulze *et al.* (1989). The advancing and receding contact angles can be regulated by changing the hysteresis angle, therefore controlling the pinning time of the contact line and then realizing the manipulation of the drop evaporation.

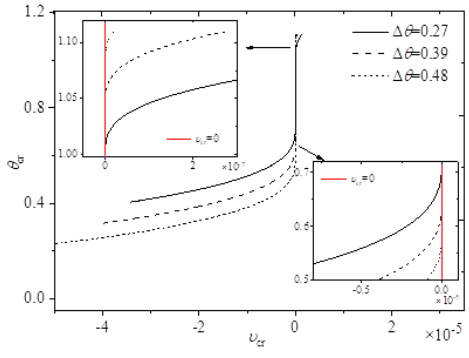

Fig. 12. Dynamic contact angle vs. the moving speed of the contact line

4. CONCLUSION

A numerical simulation of the drop evaporation on a uniformly heated surface with CAH is performed.

Table. 6. Variation in θ_a and θ_r of the drop with different $\Delta\theta$.

$\Delta\theta$	θ_a	θ_r	$\Delta\theta_a$	$\Delta\theta_r$
0.27	0.999	0.73	0.105	0.164
0.39	1.045	0.658	0.046	0.072
0.48	1.083	0.598	0.038	0.06

The evolution of an evaporating drop is governed by the capillary effect, gravity, the thermocapillary effect, and evaporation effect. At the center of the drop, gravity and evaporation act to promote in reduction of drop thickness, while the capillary and thermocapillary forces are responsible for the inhibition. At the edge of the drop, the capillary force, gravity, and evaporation promote the reduction of the drop thickness, whereas the thermocapillary force acts as inhibition, and evaporation always plays a major role.

The CAH has an apparent impact on the evaporation dynamics of drops. The drop evolution process exhibits three typical stages: spreading, pinning, and depinning of the contact line. The CAH has different effects on each stage of drop evaporation, that is, the spreading and depinning durations are shortened when considering the CAH, while the pinning duration is prolonged. In the drop spreading stage, increasing the hysteresis angle reduces the spreading velocity and the radius; thus, the drop spreading is inhibited. In the contact line pinning stage, the supplemented mass toward the contact line induced by the combined contribution of gravity, the capillary, and the thermocapillary forces is balanced with the evaporated mass, thereby realizing the dynamic balance manifested as the pinning of the contact line. The CAH can prolong the pinning time, maintain a specific solid-liquid contact area, then enhance heat transfer and accelerate evaporation. In the contact line depinning stage, the CAH declines the contact angle, and a flatter shape gradually evolves. Then the heat transfer performance is enhanced, thus accelerating evaporation and shortening the depinning time. Hence, the CAH can speed up the drying of the drop, and the large hysteresis angle leads to faster evaporation.

As the contact line starts pinning or depinning, the drop reaches the advancing contact angle or receding contact angle. A significant hysteresis angle results in a large advancing contact angle and a small receding contact angle. The receding contact angle reduction is more apparent than the increment of the advancing contact angle. Regulating the hysteresis of the contact angle effectively manipulates the contact line motion for an evaporating drop.

REFERENCES

Ajaev, V. S. (2005). Spreading of thin volatile liquid droplets on uniformly heated surfaces, *Journal of Fluid Mechanics* 528, 279-96.

Anderson, D. M. and S. H. Davis (1995). The spreading of volatile liquid droplets on heated surfaces, *Physics of Fluids* 7, 248-65.

Bonn, D., J. Eggers, J. Indekeu, J. Meunier and E. Rolley (2009). Wetting and spreading, *Reviews of modern physics* 81, 739.

Bormashenko, E., A. Musin and M. Zinigrad (2011). Evaporation of droplets on strongly and weakly pinning surfaces and dynamics of the triple line, *Colloids and Surfaces A: Physicochemical and Engineering Aspects* 385, 235-40.

Brutin, D. and B. Sobac (2015). Triple Line Motion and Evaporation. in, *Droplet Wetting and Evaporation* (Elsevier).

Chu, F. Q., X. M. Wu, Y. Zhu and Z. P. Yuan (2017). Relationship between condensed droplet coalescence and surface wettability, *International Journal of Heat Mass Transfer* 111, 836-41.

Craster, R. V., O. K. Matar and K. Sefiane (2000). Surfactant transport on mucus films, *Journal of Fluid Mechanics* 425, 235-58.

Craster, R. V., O. K. Matar and Khellil Sefiane (2009). Pinning, retraction, and terracing of evaporating droplets containing nanoparticles, *Langmuir* 25, 3601-09.

Dettre, R. H. and R. E. Johnson (1965). Contact angle hysteresis. IV. Contact angle measurements on heterogeneous surfaces, *The Journal of Physical Chemistry* 69, 1507-15.

Diddens, C., J. G. M. Kuerten, C. W. M. Van der Geld and H. M. A. Wijshoff (2017). Modeling the evaporation of sessile multi-component droplets, *Journal of Colloid and Interface Science* 487, 426-36.

Ding, H. and P. D. M. Spelt (2007). Wetting condition in diffuse interface simulations of contact line motion, *Physical Review E* 75, 046708.

Dugas, V., J. Broutin and E. Souteyrand (2005). Droplet evaporation study applied to DNA chip manufacturing, *Langmuir* 21, 9130-36.

Eral, H. B. and J. M. Oh (2013). Contact angle hysteresis: a review of fundamentals and applications, *Colloid Polymer Science*, 291: 247-60.

Gatapova, E., A. Ya., A. Semenov, D. V. Zaitsev and O. A. Kabov (2014). Evaporation of a sessile water drop on a heated surface with controlled wettability, *Colloids Surfaces A: Physicochemical Engineering Aspects* 441, 776-85.

Hoffman, R. L. (1974). A study of the advancing interface. I. Interface shape in liquid—gas systems, *Journal of Colloid and Interface Science* 50, 228-41.

Hu, D. H. and H. Y. Wu (2016). Volume evolution of small sessile droplets evaporating in stick-slip mode, *Physical Review E* 93, 042805.

Jiang, T. S., O. H. Soo-Gun and J. C. Slattery (1979). Correlation for dynamic contact angle, *Journal of Colloid and Interface Science* 69, 74-77.

Johnson, R. E. and R. H. Dettre (1964). Contact angle hysteresis. III. Study of an idealized heterogeneous surface, *The Journal of Physical Chemistry* 68, 1744-50.

Kandlikar, S. G. (2012). History, advances, and challenges in liquid flow and flow boiling heat transfer in microchannels: a critical review, *Journal of Heat Transfer* 134.

Karapetsas, G. , R. V. Craster and O. K. Matar (2011). Surfactant-driven dynamics of liquid lenses, *Physics of Fluids* 23, 122106.

Karapetsas, G. , K. C. Sahu and O. K. Matar (2016). Evaporation of sessile droplets laden with particles and insoluble surfactants, *Langmuir* 32, 6871-81.

Karapetsas, G., K. C. Sahu and O. K. Matar (2013). Effect of contact line dynamics on the thermocapillary motion of a droplet on an inclined plate, *Langmuir* 29, 8892-906.

Kavehpour, P., B. Ovryn and G. H. McKinley (2002). Evaporatively-driven Marangoni instabilities of volatile liquid films spreading on thermally conductive substrates, *Colloids Surfaces A: Physicochemical Engineering Aspects* 206, 409-23.

Kiper, I., R. Fulcrand, C. Pirat, G. Simon, B. Stutz and S. M. M. Ramos (2015). Sessile drop evaporation on (super)hydrophobic surfaces: Effect of low pressure on the contact line dynamics, *Colloids and Surfaces A: Physicochemical and Engineering Aspects* 482, 617-23.

Kulinich, S. A. and M. Farzaneh (2009). Effect of contact angle hysteresis on water droplet evaporation from super-hydrophobic surfaces, *Applied Surface Science* 255, 4056-60.

Kuznetsov, G. V., D. V. Feoktistov, E. G. Orlova and K. A. Batishcheva (2016). Regimes of water droplet evaporation on copper substrates, *Colloid Journal* 78, 335-39.

Lee, K. S., N. Ivanova, V. M. Starov, N. Hilal and V. Dutschk (2008). Kinetics of wetting and spreading by aqueous surfactant solutions, *Advances in Colloid and Interface Science* 144, 54-65.

Li, Y. F., Y. J. Sheng and H. K. Tsao (2013). Evaporation stains: suppressing the coffee-ring effect by contact angle hysteresis, *Langmuir* 29, 7802-11.

Lin, T. S., Y. H. Zeng, R. Y. Tsay and S. Y. Lin (2016). Roughness-induced strong pinning for drops evaporating from polymeric surfaces, *Journal of the Taiwan Institute of Chemical Engineers* 62, 54-59.

Lopes, M. C. and E. Bonaccurso (2012). Evaporation control of sessile water drops by soft viscoelastic surfaces, *Soft Matter* 8, 7875-81.

Matar, O. K. and R. V. Craster (2009). Dynamics and stability of thin liquid films, *Reviews of modern physics* 81, 1131.

Nagy, M. and J. Škvarla (2013). Determination of contact angle hysteresis of water microdroplets evaporating on hydrolyzed PET foils, *Acta Montanistica Slovaca* 18, 125-28.

Neumann, A. W. and R. J. Good (1972). Thermodynamics of contact angles. I. Heterogeneous solid surfaces, *Journal of Colloid and Interface Science* 38 341-58.

Orlova, E. G., D. V. Feoktistov, G. V. Kuznetsov and K. O. Ponomarev (2018). Spreading of a distilled water droplet over polished and laser-treated aluminum surfaces, *European Journal of Mechanics-B/Fluids* 68, 118-27.

Oron, A., S. H. Davis and S. G. Bankoff (1997). Long-scale evolution of thin liquid films, *Reviews of Modern Physics* 69, 931.

Pan, Z. H., J. A. Weibel and S. V. Garimella (2020). Transport mechanisms during water droplet evaporation on heated substrates of different wettability, *International Journal of Heat Mass Transfer* 152, 119524.

Pasandideh-Fard, M., S. D. Aziz and S. Chandra (2001). Cooling effectiveness of a water drop impinging on a hot surface, *International Journal of Heat and Fluid Flow* 22, 201-10.

Pham, T. and S. Kumar (2019). Imbibition and evaporation of droplets of colloidal suspensions on permeable substrates, *Physical Review Fluids* 4, 034004.

Picknett, R. G. and R. Bexon (1977). The evaporation of sessile or pendant drops in still air, *Journal of Colloid and Interface Science* 61, 336-50.

Pournaderi, P. and M. Emdadi (2019). Study of droplet impact on a wall using a sharp interface method and different contact line models, *Journal of Applied Fluid Mechanics* 12, 1001-12.

Putnam, S. A., A. M. Briones, L. W. Byrd and J. S. Ervin (2012). Microdroplet evaporation on superheated surfaces, *International Journal of Heat Mass Transfer* 55, 5793-807.

Saada, M. A., S. Chikh and L. Tadrist (2010). Numerical investigation of heat and mass transfer of an evaporating sessile drop on a horizontal surface, *Physics of Fluids* 22, 13.

Schulze, R. D., W. Possart and H. Kamusewitz (1989). Young's equilibrium contact angle on rough solid surfaces. Part I. An empirical determination, *Journal of Adhesion Science Technology* 3, 39-48.

Sefiane, K., S. K. Wilson, S. David, G. J. Dunn and B. R. Duffy (2009). On the effect of the

atmosphere on the evaporation of sessile droplets of water, *Physics of Fluids* 21, 9.

Semenov, S., V. M. Starov, R. G. Rubio, H. Agogo and M. G. Velarde (2012). Evaporation of Sessile Water Droplets in Presence of Contact Angle Hysteresis, *Mathematical Modelling of Natural Phenomena* 7, 82-98.

Smith, M. K. (1995). Thermocapillary migration of a two-dimensional liquid droplet on a solid surface, *Journal of Fluid Mechanics* 294, 209-30.

Trybala, A., A. Okoye, S. Semenov, H. Agogo, R. G. Rubio, F. Ortega and V. M. Starov (2013). Evaporation kinetics of sessile droplets of aqueous suspensions of inorganic nanoparticles, *Journal of Colloid and Interface Science* 403, 49-57.

Wang, X. D., X. F. Peng, J. F. Lu and B. X. Wang (2003). Measuring Technique of Contact Angle and Contact Angle Hysteresis on Rough Solid Surfaces Ⅱ: Contact Angle Hysteresis on Rough Stainless Steel, *Journal of basic science and engineering(in Chinese)*, 296-303.

Wijshoff, H. (2010). The dynamics of the piezo inkjet printhead operation, *Physics Reports* 491, 77-177.

Xu, X. M. and X. P. Wang (2020). Theoretical analysis for dynamic contact angle hysteresis on chemically patterned surfaces, *Physics of Fluids* 32, 10.

Ye, X. M., X. S. Zhang, M. L. Li and C. X. Li (2018). Dynamics of self-rewetting drop on an inclined uniformly heated substrate, *Physics of Fluids* 30, 112103.

Ye, X. M., X. S. Zhang, M. L. Li, C. X. Li and S. Dong (2019). Contact line dynamics of two-dimensional evaporating drops on heated surfaces with temperature-dependent wettabilities, *International Journal of Heat Mass Transfer* 128, 1263-79.

Yin, L. F., A. Chauhan, A. Recinella, L. Jia and S. G. Kandlikar (2020). Subcooled flow boiling in an expanding microgap with a hybrid microstructured surface, *International Journal of Heat Mass Transfer* 151, 119379.

Yu, H. Z., Di. M. Soolaman, A. W. Rowe and J. T. Banks (2004). Evaporation of Water Microdroplets on Self‐Assembled Monolayers: From Pinning to Shrinking, *ChemPhysChem* 5, 1035-38.

Zhang, C. Y., H. Zhang, X. S. Zhang, C. Yang and P. Cheng (2021). Evaporation of a sessile droplet on flat surfaces: An axisymmetric lattice Boltzmann model with consideration of contact angle hysteresis, *International Journal of Heat and Mass Transfer* 178, 121577.